Supporting Information for

The Strong Confinement Regime in HgTe Two-Dimensional Nanoplatelets

Nicolas Moghaddam[1], Charlie Gréboval[2], Junling Qu[2], Audrey Chu[2], Prachi Rastogi[2], Clément Livache[2], Adrien Khalili[1], Xiang Zhen Xu[1], Benoit Baptiste[3], Stefan Klotz[3], Guy Fishman[4], Francesco Capitani[5], Sandrine Ithurria[1], Sébastien Sauvage[6*], Emmanuel Lhuillier[2*]

[1]Laboratoire de Physique et d'Etude des Matériaux, ESPCI-ParisTech, PSL Research University, Sorbonne Université UPMC Univ Paris 06, CNRS, 10 rue Vauquelin 75005 Paris, France.

[2]Sorbonne Université, CNRS, Institut des NanoSciences de Paris, INSP, F-75005 Paris, France.

[3]Sorbonne Université, CNRS, Institut de Minéralogie, de Physique des Matériaux et de Cosmochimie, IMPMC, F-75005 Paris, France.

[4]Kadope, Centre de Nanosciences et de Nanotechnologies, 10 boulevard Thomas Gobert, 91120, Palaiseau, France.

[5]Synchrotron-SOLEIL, Saint-Aubin, BP48, F91192 Gif sur Yvette Cedex, France.

[6]Université Paris-Saclay, CNRS, Centre de Nanosciences et de Nanotechnologies, 91120, Palaiseau, France.

*To whom correspondence should be sent: el@insp.upmc.fr and sebastien.sauvage@c2n.upsaclay.fr

Table of content

I. MATERIALS 2

1.1. Synthesis of HgTe Nanoplatelets 2

1.2. Synthesis of HgTe nanocrystals 5

2. Material characterization 7

3. Infrared spectroscopy 8

3.1. Infrared spectroscopy as a function of temperature 8

3.2. Infrared spectroscopy under pressure: 9

4. Multiband k.p modelling 10

4.1 Simple (3+1)-band model 10

4.2 Bulk HgTe band gap variations with temperature and pressure 11

4.3 Modeling of strong confinement 11

4.4 Effect of temperature on the second conduction band 12

4.5 Detailed discussion on the effect of pressure, notably at low energies (≈ 0.5–0.7 eV) 13

4.6 Realistic 14-band k.p model 14

4.7 Conclusion 18

5. REFERENCES 19

I. MATERIALS

1.1. Synthesis of HgTe Nanoplatelets

The growth of the HgTe nanoplatelets (NPLs) follows the procedure developed by Izquierdo et al.[1] The process starts with the synthesis of CdTe NPLs and cations (Cd→Hg) are then exchanged.

Synthesis of 3 MLs CdTe NPLs: The obtained NPLs present a first excitonic feature at 500 nm (2.48 eV), see Figure S 1a. Their thickness corresponds to 3 monolayers (3 planes of Te sandwiched between 4 planes of Cd). Their lateral extension reached several hundred of nm, see microscopy image in Figure S 1b.

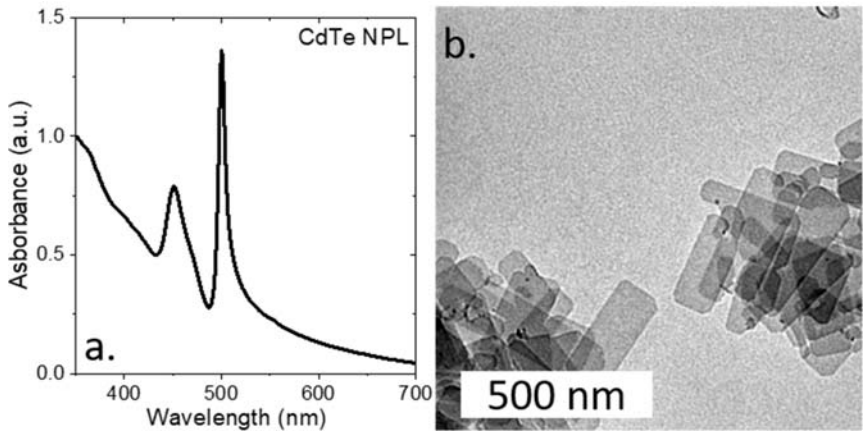

Figure S 1 a. Room temperature absorption spectrum of CdTe NPLs. b. Tranmission electron microscopy image of CdTe NPLs.

Cation exchange for synthesis of 3 MLs HgTe NPLs with TOA: After the cation exchange process, the X-ray diffractogram stay almost unchanged, see Figure S 2. The change of Scherrer size as material is transformed from CdTe to HgTe is less than 2%

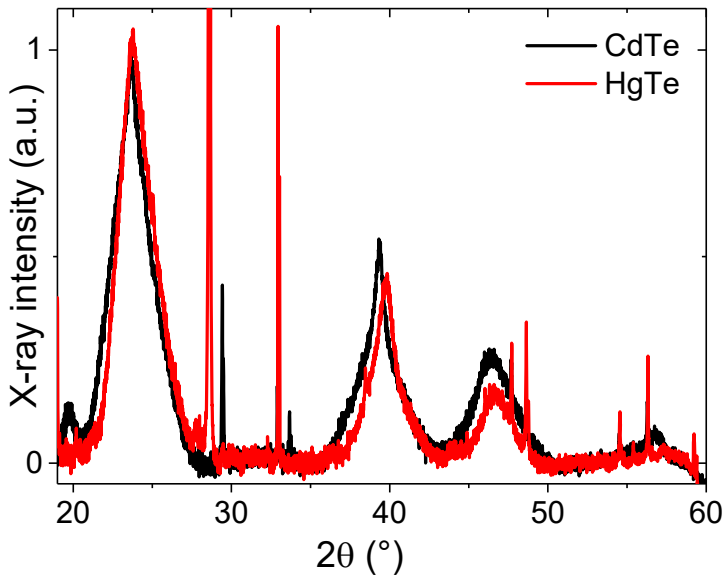

Figure S 2 X-ray diffraction pattern for CdTe and HgTe NPLs.

The first excitonic feature of the HgTe NPL is strongly redshifted with respect to the CdTe NPL, reaching now 850 nm (1.46 eV), see Figure S 3a. The lateral extension is mostly unchanged, see Figure S 3b.

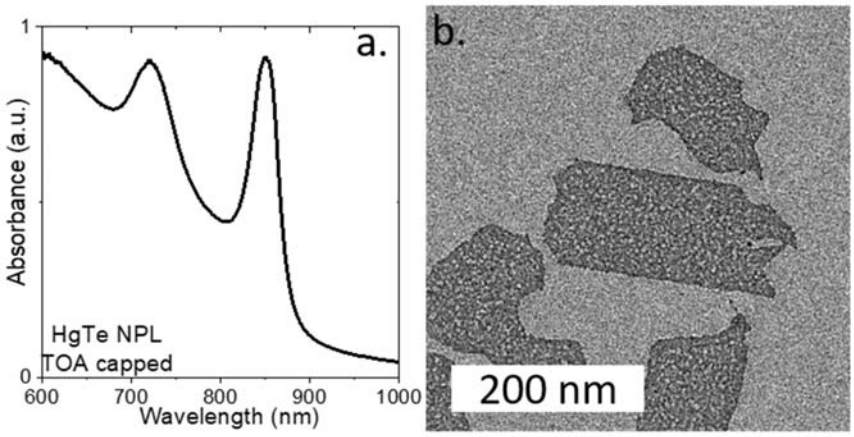

Figure S 3 a. Room temperature absorption spectrum of HgTe NPLs capped with trioctylamine (TOA). b. Transmission electron microscopy image of HgTe NPLs capped with TOA.

Cation exchange and ligand exchange for synthesis of X capped 3MLs HgTe NPLs (X= Br, I): In a glass tube, 2 mL of toluene and 150 µL of CdTe NPLs are introduced. 15 µL of a fresh 0.25 M $HgAc_2$ in oleylamine solution is added at room temperature (Cd:Hg ratio is 1:2). The cation exchange is followed by absorption spectroscopy. Once the first excitonic peak has reached 850 nm, 20 µL of a fresh 0.25 M HgX_2 in oleylamine solution is added at room temperature ($Hg_{(s)}$:X ratio is 1:10). The ligand exchange is followed by absorption spectroscopy. Once the first excitonic peak has reached 925 nm for X=Br or 930 nm for X = I and 5 µL of oleylamine are added. The excess of precursor is removed by centrifugation (5000 rpm, 2 min). The resulting nanoplatelets are resuspended in 1 mL of toluene. After the cation exchange process, the first excitonic feature is strongly redshifted, reaching now 928 nm (1.34 eV), see Figure S 4a. Even though still 2D the shape of the particles can be affected by this approach in the case of Br, see Figure S 4b.

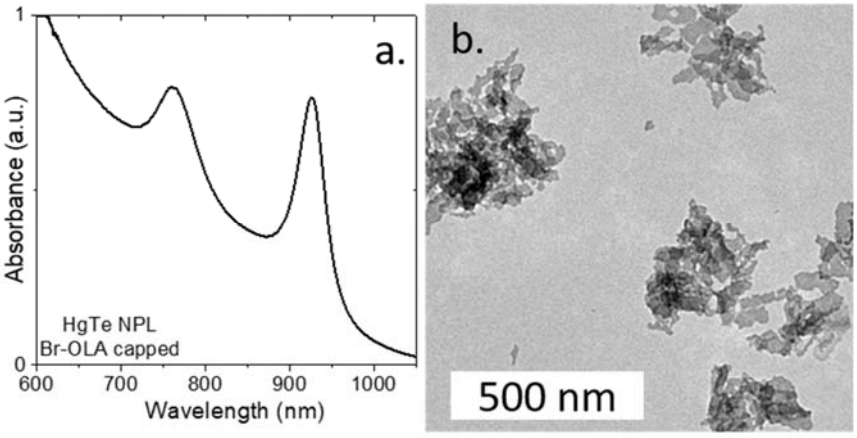

Figure S 4 a. Room temperature absorption spectrum of HgTe NPLs capped with Br coupled to Oleylamine (OLA). b. Transmission electron microscopy image of HgTe NPLs capped with Br coupled to OLA.

When I is used instead of Br, the excitonic is located at 933 nm (1.33 eV), see Figure S 5a, but the shape is better preserved, see Figure S 5b.

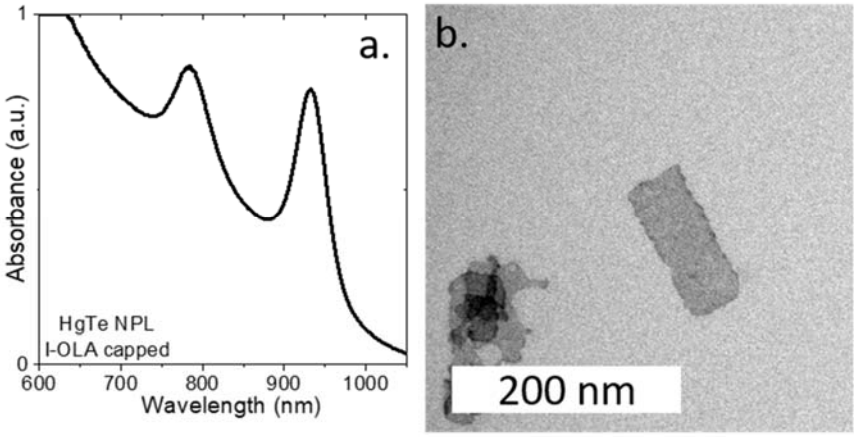

Figure S 5 a. Room temperature absorption spectrum of HgTe NPLs capped with I coupled to Oleylamine (OLA). b. Transmission electron microscopy image of HgTe NPLs capped with I coupled to OLA.

1.2. Synthesis of HgTe nanocrystals

HgTe NCs synthesis with band edge at 9000 cm^{-1}: In a 25 mL three neck flask, 270 mg of $HgCl_2$ and 10 mL of oleylamine are degassed under vacuum at 110 °C. At this stage, the solution is yellow and clear. While 1 mL of TOP:Te solution (1 M) is extracted from glove box, the temperature is set at 60 °C and the atmosphere is switched to Ar. When the temperature is stable, the TOP:Te solution is quickly injected. The solution turns into coffee-like color after 40 sec. After 50 sec, 5 mL of a cold mixture of DDT in toluene (20% of DDT) with 4 drops of TOP is injected and the temperature is decreased with air flux. The content of the flask is transferred in a weighted falcon. Addition of absolute EtOH followed by centrifugation leads to a dark precipitate that is redispersed in toluene. The solution is precipitated a second time using absolute EtOH, centrifugated and the dark pellet is redispersed in toluene and filtrated with 0.2 µm filter. Absorption and TEM image of the obtained material can be seen in Figure S 6a.

HgTe NCs synthesis with band edge at 8000 cm^{-1}: The reaction is taken from Geiregat *et al*.[2] 270 mg (1 mmol) of $HgCl_2$, 1.6 ml (6 mmol) of dodecanethiol (DDT), and 8 mL of oleylamine (OLA) were mixed in a 25 mL flask. The flask is degassed under vacuum at 100 °C for 1 h. The reaction mixture was placed under Ar while keeping the temperature at 60 °C. Next, 1 mL of a 1 M solution of TOP:Te (1M) was rapidly injected and a black-colored reaction mixture was obtained within a few seconds. The reaction mixture was kept at the injection temperature to allow for QD growth for 1 min (PL is expected to be at 1220 nm). The reaction was quenched by injecting 10 mL of toluene and cooling with a water bath. As-obtained HgTe QDs were purified twice using toluene and methanol. The pellet is redispersed in 7.5 mL of toluene. The nanocrystals (NCs) are then centrifuged in pure toluene to remove non-colloidally stable material. The supernatant is filtered. Absorption and TEM image of the obtained material can be seen in Figure S 6b.

HgTe NCs synthesis with band edge at 6000 cm^{-1}: The reaction is taken from Keuleyan *et al*.[3] 513 mg of $HgCl_2$ was added to 60 mL of oleylamine in a 100 mL round flask. The solution was placed under vacuum and heated to 110 °C for 1 h. Then, the temperature is decreased to 60 °C and solution is placed to Ar atmosphere. 1.9 mL of TOP:Te (1 M) with 10 mL of oleylamine is added to the mercury solution. The solution color gradually turns to dark brown and the reaction is stopped at 3 min. A solution made of 1 mL of dodecanethiol and 9 mL of toluene is quickly added to quench the reaction. The nanocrystals are then precipitated with ethanol. After centrifugation, the nanocrystals are redispersed in chloroform. The washing step is repeated one more time. The solution is redispersed in chloroform and filtered with a 0.2 µm filter. Additional two washing steps are applied with final redispersion in chloroform. Absorption and TEM image of the obtained material can be seen in Figure S 6c.

HgTe NCs synthesis with band edge at 4000 cm^{-1}: Absorption and TEM image of the obtained material can be seen in Figure S 6d.

HgTe NCs synthesis with band edge at 2000cm^{-1}: 513 mg of $HgCl_2$ was added to 60 mL of oleylamine in a 100 mL round flask. The solution was placed under vacuum and heated to 110 °C for 1 h. Then, the temperature is increased to 120 °C and solution placed to Ar atmosphere. 1.9 mL of TOP:Te (1 M) with 10 mL of oleylamine is added to the mercury solution. The solution color gradually turns to dark brown and the reaction is stopped at 3 min. A solution made of 1 mL of dodecanethiol and 9 mL of toluene is quickly added to quench the reaction. The nanocrystals are then precipitated with ethanol. After centrifugation, the nanocrystals are redispersed in chloroform. The washing step is repeated one more time. Absorption and TEM image of the obtained material can be seen in Figure S 6e.

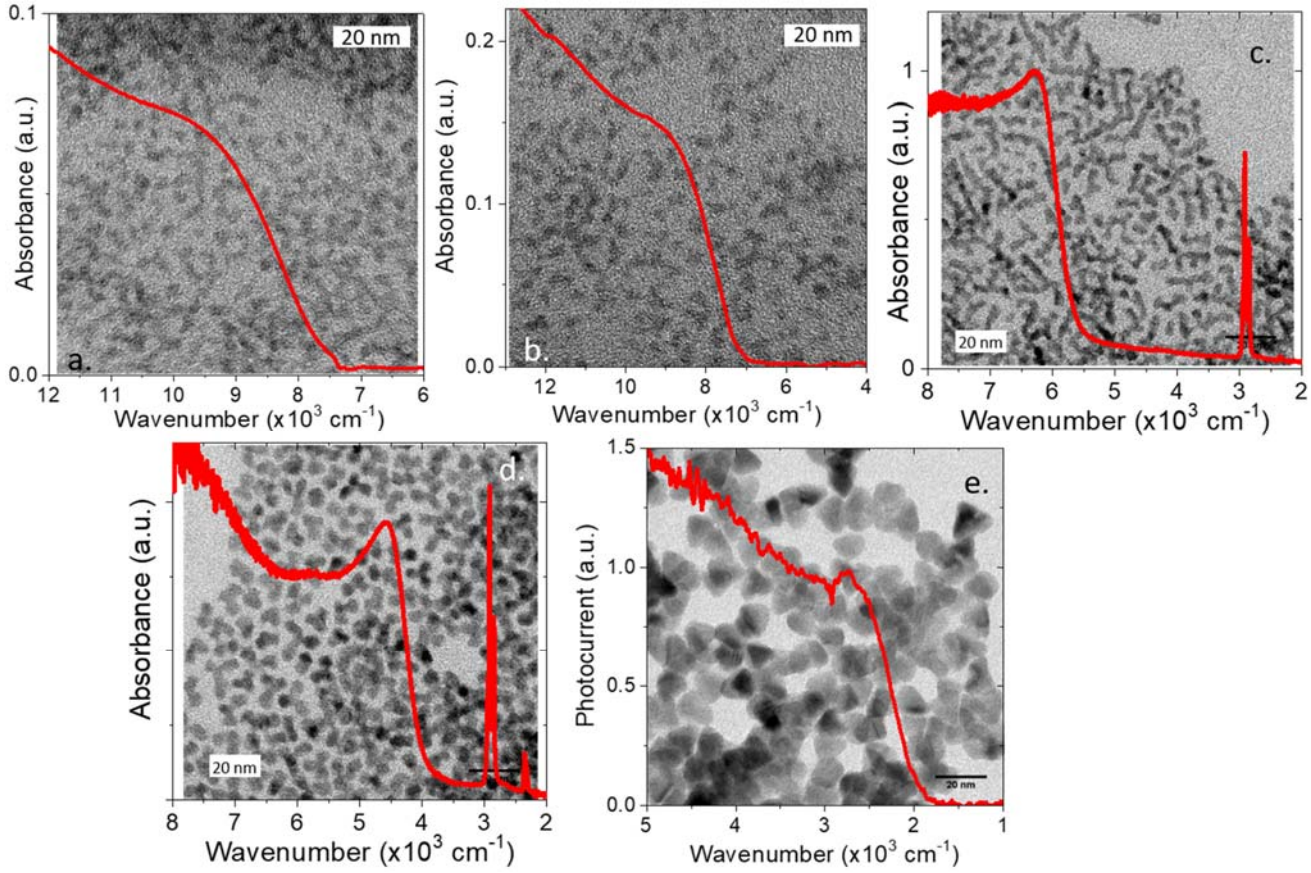

Figure S 6 a. Room temperature absorption spectrum for HgTe NCs with a band edge at 9000 cm^{-1}. The associated TEM image is used as background. b. Room temperature absorption spectrum for HgTe NCs with a band edge at 8000 cm^{-1}. The associated TEM image is used as background. c. Room temperature absorption spectrum for HgTe NCs with a band edge at 6000 cm^{-1}. The associated TEM image is used as background. d. Room temperature absorption spectrum for HgTe NCs with a band edge at 4000 cm^{-1}. The associated TEM image is used as background. e. Room temperature absorption spectrum for HgTe NCs with a band edge at 2000 cm^{-1}. The associated TEM image is used as background.

2. Material characterization

X-ray diffraction under pressure: The diffraction pattern for HgTe NPLs is shown in Figure S 7a-b. The lattice parameter in the zinc blende phase is reported as a function of pressure in Figure S 7c.

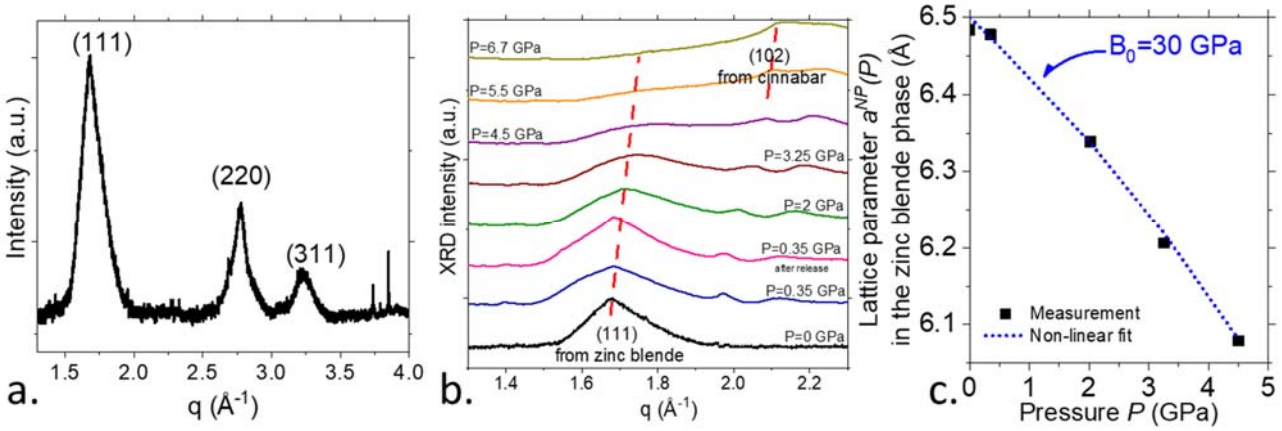

Figure S 7 a. X-ray diffraction pattern of HgTe NPL under zero pressure b. X-ray diffraction pattern of HgTe NPL around the (111) peak of the zinc blende phase under various pressure. c. Lattice parameter of the zinc blende phase as a function of an applied pressure P, at room temperature.

To use it in the **k.p** modelling, we fit the lattice parameter following:

$$a^{NP}(T = 300K, P) = a_0^{NP}\left(1 - \frac{P}{3(B_0 - 1.5P)}\right)$$

with P in GPa. $a_0^{NP} = 6.50$ Å is the HgTe nanoparticle lattice parameter at zero pressure and B_0=30 GPa the apparent elasticity modulus at zero pressure. The fit is plotted in Figure S 6c as a blue dotted line. The bulk lattice constant of HgTe being $a_0 = 6.4605$ Å at room temperature,[4] the NPLs exhibit a slight initial tensile strain, resulting in a slightly larger lattice parameter a_0^{NP}. This tensile strain is attributed to the presence of ligands, giving rise to twisted NPLs as in [5] . The zero-pressure bulk modulus $B_0 = 30$ GPa is closed to the one of bulk HgTe of 33 GPa.[6] The lattice parameter exhibits a non-linear dependence with pressure, indicating that the bulk modulus lightly decreases with pressure too.

3. Infrared spectroscopy

3.1. Infrared spectroscopy as a function of temperature

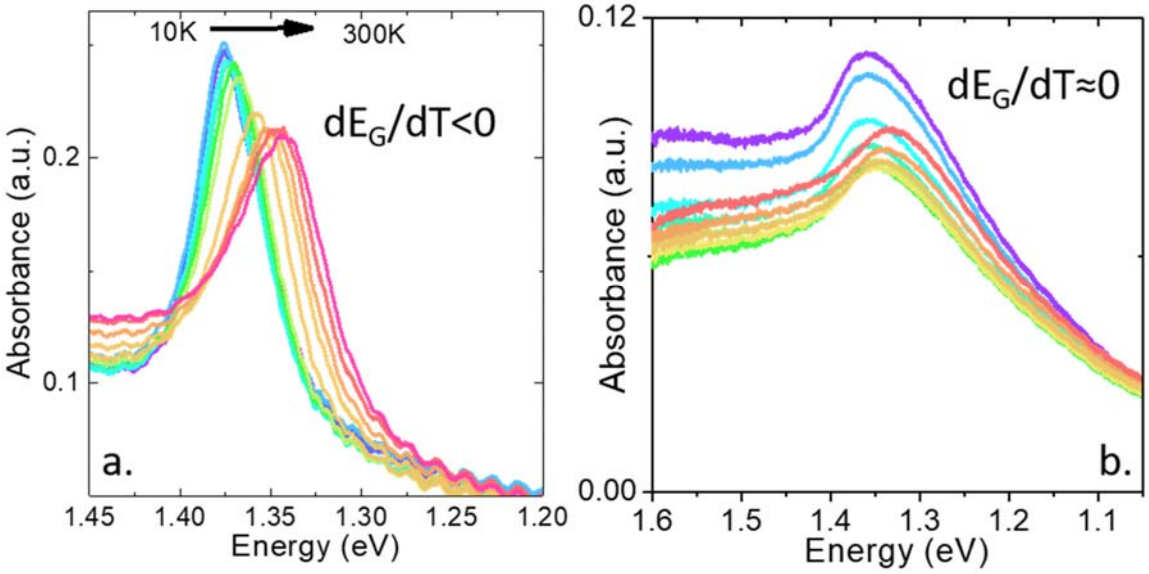

Figure S 8 a. Absorption spectra of HgTe NPLs capped with Br coupled to Oleylamine for various temperatures between 10 K and 300 K. b. Absorption spectra of HgTe NPLs capped with I coupled to Oleylamine for various temperatures between 10 K and 300 K.

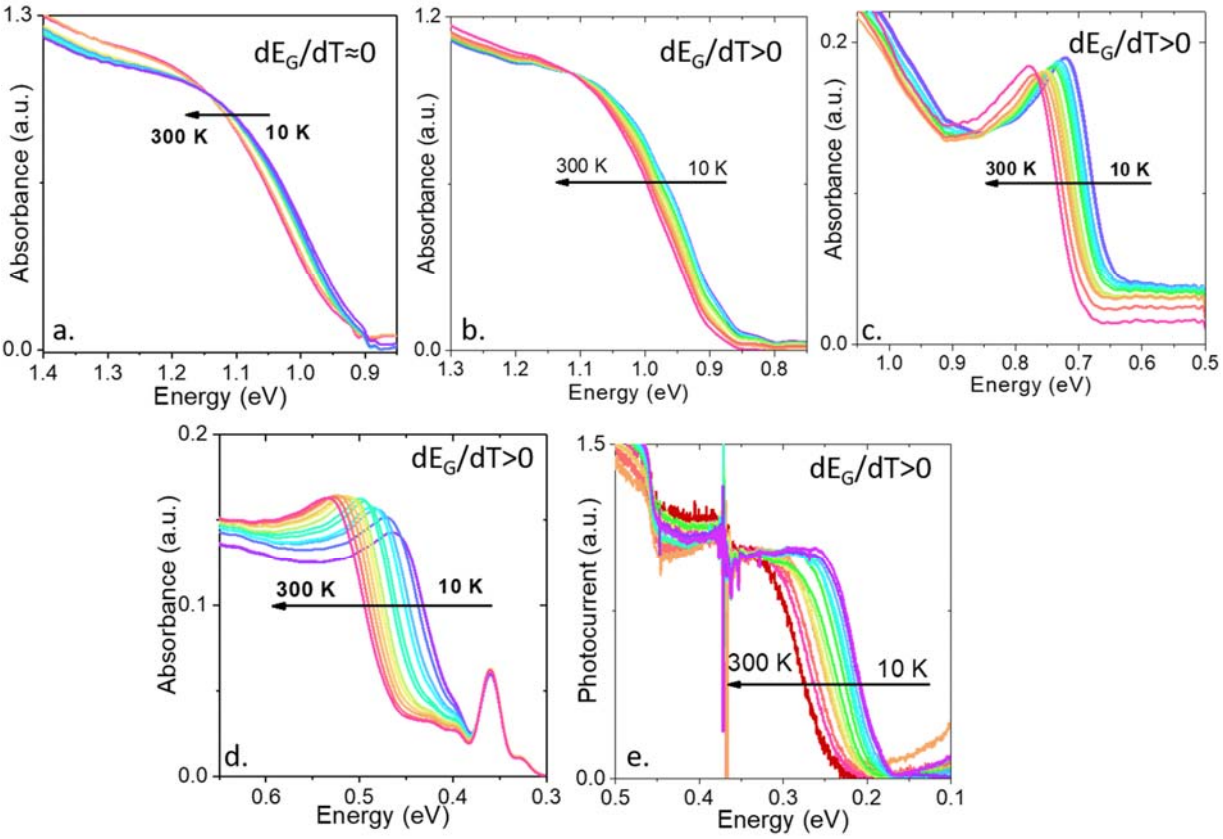

Figure S 9 Absorption spectra for HgTe NCs with a band edge at a. 9000 cm^{-1}, b. 8000 cm^{-1}, c. 6000 cm^{-1}, d. 4000 cm^{-1} and e. 2000 cm^{-1} for various temperature between 10 K and 300 K. The feature at 0.36 eV corresponds to the absorption from the C-H bond.

3.2. Infrared spectroscopy under pressure:

Figure S *10* presents the infrared spectra acquired under various applied pressure and temperature.

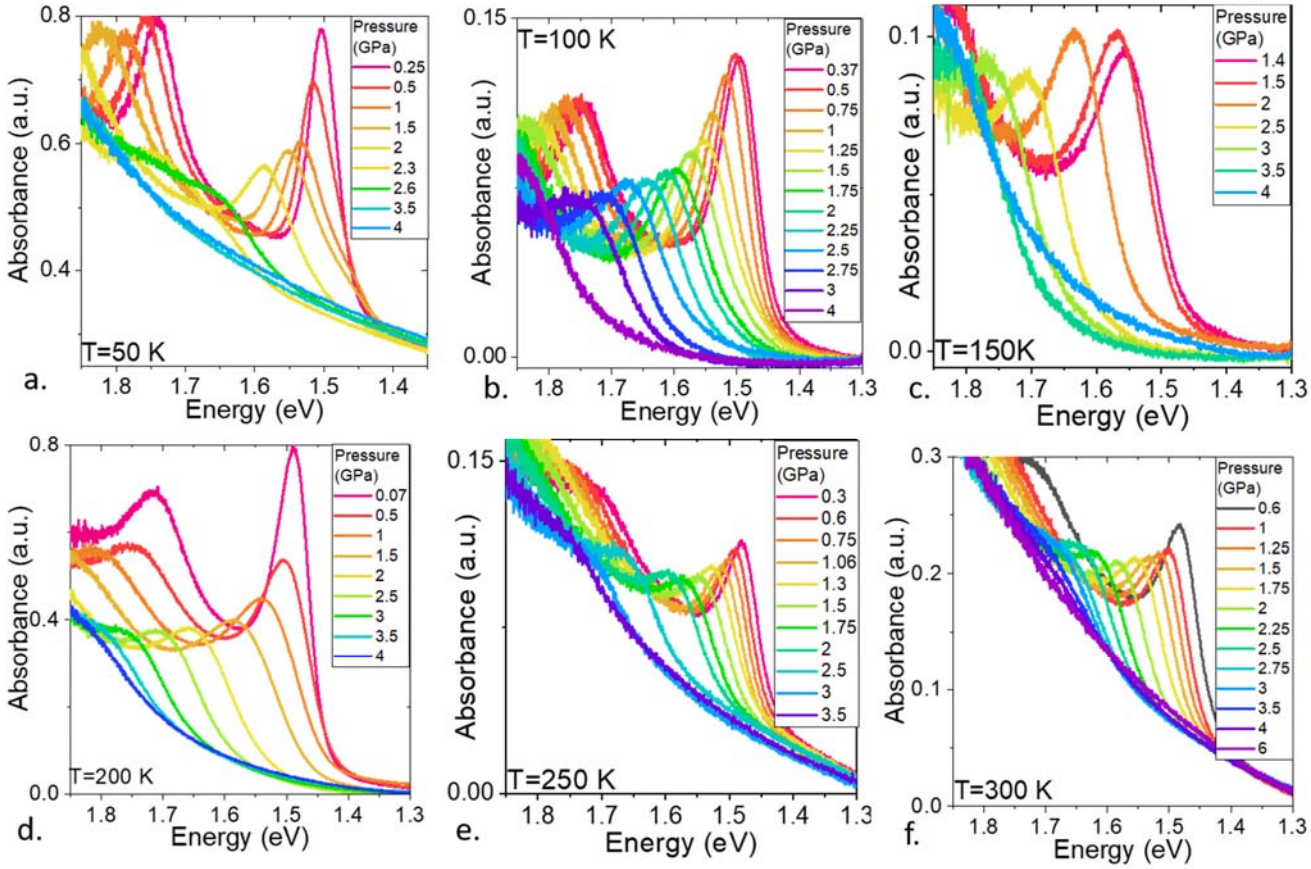

Figure S *10* Infrared spectra of HgTe NPLs under various applied pressure, measured at a. 50, b. 100, c. 150, d. 200, e. 250, and f. 300 K.

4. Multiband k.p modelling

Introduction. In order to account for the temperature and pressure dependent spectroscopies observed experimentally, we model the nanoparticles energies using a combination of multiband k.p simulations and straightforward treatment of the strong confinement in the reciprocal space. The core ingredients in these models are the two band gaps E_g and E_{gC}:

- E_g between the LH conduction band and the second valence electron E band (Γ_6 symmetry in HgTe crystal)
- E_{gC} from the first LH conduction band and the second conduction band of HgTe

We use a simple k.p-like model for the discussion in the main text and a 14-band k.p model for a more detailed discussion and to support the simple model more realistically.

4.1 Simple (3+1)-band model

In this simple effective model, we include the minimal number of interactions between bands to represent the effective contributions of all the bands on the electronic dispersion relation $E(k)$, possibly outside the projection basis. For the light hole like (LH) conduction band, we use a 3-band hamiltonian and a parabolic dispersion for the heavy-hole like (HH) valence band:

$$\widehat{H}(k) = \begin{bmatrix} E_{gC} & k\,P_C & k\,P_V \\ k\,P_C & 0 & k\,P \\ k\,P_V & k\,P & -E_g \end{bmatrix} + \frac{\hbar^2 k^2}{2m_0} Id_3 \qquad \text{(S1)}$$

$$E_{LH}(k) = 2^{\text{nd}} \text{ eigen energy of } \widehat{H}$$

and

$$E_{HH}(k) = -\frac{\hbar^2 k^2}{2m^*_{HH}} \qquad \text{(S2)}$$

with E_g, E_{gC} 2 band bap energies, $k\,P = \sqrt{E_p \frac{\hbar^2 k^2}{2m_0}}$, $k\,P_C = \sqrt{E_{pC} \frac{\hbar^2 k^2}{2m_0}}$, $k\,P_V = \sqrt{E_{pV} \frac{\hbar^2 k^2}{2m_0}}$ 3 interaction energies, $\hbar = h/(2\pi)$ the reduced Plank constant, m_0 the free electron mass , $k = \|\vec{k}\|$ and Id_3 the 3x3 identity matrix. m^*_{HH} is the valence band effective mass. For simplicity and value change discussion, all parameters have been chosen real and positive.

Conduction band. The conduction band is coupled to the second conduction band at E_{gC} energy with E_{pC} interaction. The output dispersions $E(k)$ are reported in Fig. 4a in the main text. One notes that $E_{LH}(k)$ is highly non-parabolic, almost linear and exhibits two opposite concavities at small and large k as observed in QSGW modelling.[7] The effective mass of the conduction band can be extracted from the perturbation solution at small k using Luttinger-Kohn renormalization[8] (same equation (1) in the main text):

$$E_{LH}(k,T,P) \simeq \left(1 + \frac{E_p}{Eg(T,P)} - \frac{E_{pC}}{E_{gC}(T,P)}\right)\frac{\hbar^2 k^2}{2m_0} = \frac{\hbar^2 k^2}{2m^*_{LH}} \qquad \text{(S3)}$$

This leads to $m^*_{LH} = 0.013 m_0$ at T = 0 K and P = 0 GPa corresponding roughly to the 0.011_{m_0} mass predicted along $\Gamma - X$ by the hybrid QSGW theory of Ref. [7]. It is apparent in this expression that the second conduction band plays an opposite role as compared to the LH conduction band. When temperature is changed or pressure is applied, the 2 bands gaps are varied, modifying the electronic structure. It is clear from Figures S10b and S10c that temperature plays a different role than pressure on the confinement energy E_G. When temperature increases, E_G first shows blue-shift and then exhibits red-shift due to the "repelling" of the second conduction band getting closer. In contrast, when pressure is applied, E_G always presents blue-shift.

Valence band. The heavy hole (HH) valence band exhibits a mass $m^*_{HH} = -0.33m_0$ also in agreement with Ref. [7]. Due to the HH mass around 30 times heavier than for LH band, the HH band contribution to the confinement energy is expected to remain small, at least at small k as confirmed the realistic 14-band model (see Figure S 12b,c). Therefore, the valence band is taken as a static gap-independent parabolic band.

4.2 Bulk HgTe band gap variations with temperature and pressure

The band gap $E_g(T,P)$ of bulk HgTe varies according to the experimental measurements in bulk HgTe of Ref. [9] with temperature T, and linearly with pressure P:

$$E_g(T,P) = E_g^0 - \left(6.3\ 10^{-4}\frac{T^2}{11+T}\right) + \frac{\partial E_g}{\partial P}P \text{ (in eV)} \quad \text{(S4)}$$

The second conduction band separation is taken with linear dependences:

$$E_{gC}(T,P) = E_{gC}^0 + \frac{\partial E_{gC}}{\partial T}T + \frac{\partial E_{gC}}{\partial P}P \quad \text{(S5)}$$

as plotted in Figure S 11c and potentials (slopes) given in Table 1 in the main text.

4.3 Modeling of strong confinement

The strong confinement in the HgTe nanoparticles is modeled by the discretization of the $\vec{k}$ wavevector in the reciprocal space, typically at $k = \pm\frac{\pi}{L}$ along [001] where L is size of the nanoparticle. This crude but not so unrealistic and fruitful approach assumes that the confinement volume is bounded by infinitely high energy barriers[10] and defined by a simplified geometry. The NPL excitons are clearly confined along [001] directions. The nanocrystal (NC) geometry is simplified into a cubic quantum box. Because of the {111} surfaces growing slower than other surfaces[3] we take the cube faces parallel to {111} crystallographic planes, hence a discretization of $\vec{k}$ along <001>. The general good agreement between the 2 models and the experimental data suggests that the <001> directions are the relevant confinement directions for the NCs. The dispersion $E_{LH}(\vec{k})$ is indeed significantly anisotropic at high energy according to QSGW description[7] and following tight-binding modeling[11] or 14-band k.p modeling along other directions than <001> (not shown).

The lattice parameter $a^{NP}(T,P)$ variation, with temperature and under pressure, induces a proportional variation in the confinement size L and hence an inversely proportional change in the discretized wave vector. This strain effect comes in addition to the contraction and dilation of the Brillouin zone and subsequent energy alterations in the **k.p** modelling following.[12] We take

$$k(T,P) = k_0\frac{a^{NP}(T=0,P=0)}{a^{NP}(T,P)} \quad \text{(S6a)}$$

where k_0 is the wave vector at $T = 0$ K and P =0 GPa. We separate temperature and pressure dependences. Concerning the pressure dependence of a^{NP}, we take the measured one at room temperature in Figure S 7c and we assume it for all temperatures. Concerning temperature dependence of a^{NP}, we evaluate it at all pressures from the measurement of the linear expansion coefficient $\alpha_L(T)$ for HgTe at 0 GPa in Ref. [4] and plotted in Figure S 11a. The lattice parameter is then recovered by the integration: $a^{NP}(T,P=0)/a^{NP}(T=0,P=0) = \exp\left(\int_0^T \alpha_L(T')\mathrm{d}T'\right)$ plotted in Figure S 11b. The discretized wave vector along <001> hence reads:

$$k(k_0,T,P) = k_0\frac{1}{\left(1-\frac{P}{3(B_0-1.5P)}\right)}\frac{1}{\exp\left(\int_0^T \alpha_L(T')\mathrm{d}T'\right)} \quad \text{(S6b)}$$

a^{NP} exhibits only a maximum 0.1 % non-monotonous change over the investigated 300 K range of temperatures. A pressure up to 4 GPa induces a monotonous 6% change in a^{NP} as show in Figure S 7c, two orders of magnitude larger.

The $E_G(k,T,P)$ confinement energy is then taken as the difference between the LH energy and HH energy:

$$E_G(k,T,P) = E_{LH}(k,T,P) - E_{HH}(k,T,P) \quad \text{(S6c)}$$

The correspondence between E_G and k is given in Figure S 11d at 0 K or equivalently in Figure S 11e at 0 GPa. The temperature and pressure dependences of the electronic structure produce an alteration of E_G. For temperature analysis, when the HgTe nanoparticles are heated from 0 K up to 300 K, the simple model accounts for a blue shift at low energy for the nanocrystals and a red shift at high energy for the nanoplatelets. This is in strong contrast with simulated pressure dependence which shows only a blue shift when pressure increases.

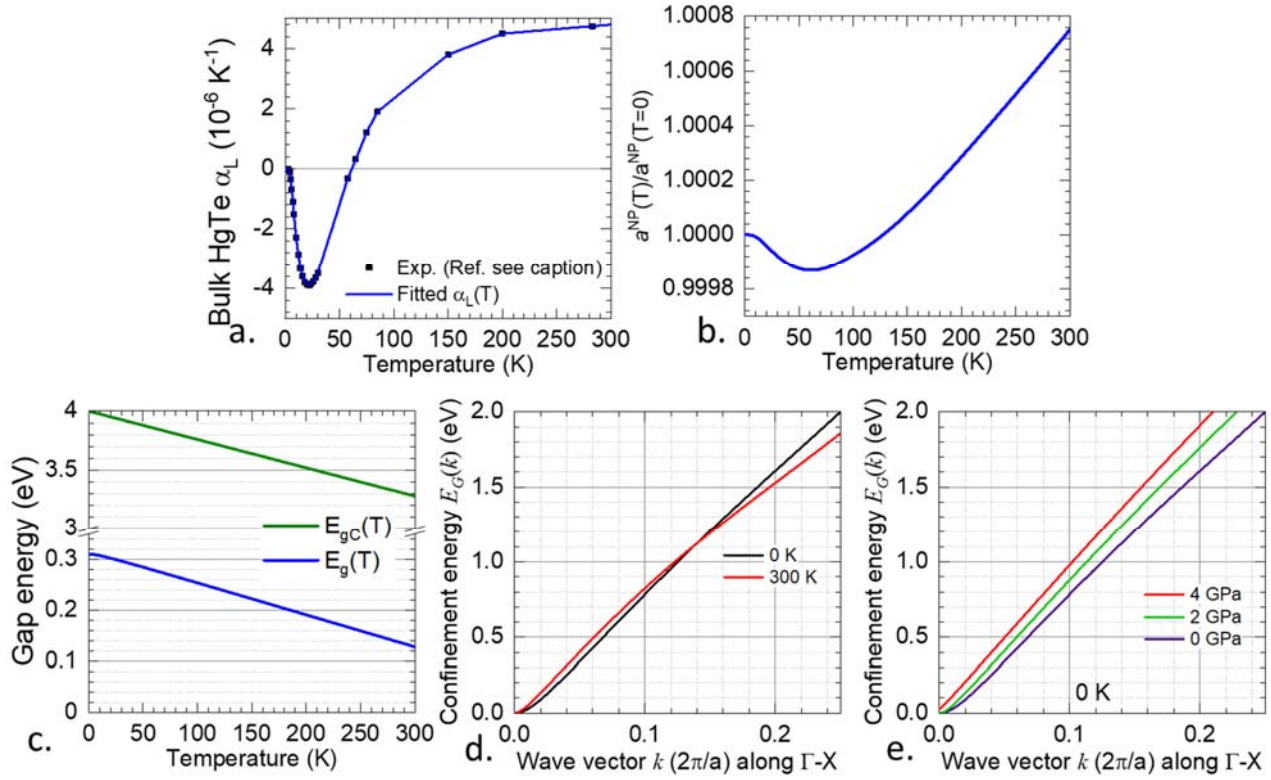

Figure S 11a. Linear expansion coefficient $\alpha_L(T)$ fitted from Ref. [4] b. Corresponding HgTe nanoparticle dilation as a function of temperature. c. Temperature dependence of gap energies $E_g(T)$ and $E_{gC}(T)$ used in the simple model. d. Simulated confinement energy $E_G(k)$ as a function of wave vector norm k for 2 temperatures T in the simple model. The thermal dilation of the k wave vector is ignored. e. Simulated confinement energy $E_G(k)$ for various pressure P in the simple model. The contraction of the k wave vector due to pressure is ignored.

4.4 Effect of temperature on the second conduction band

The effect of temperature on the IR spectrum of the material is reported in Figure S11 by providing the experimental shift of the band-edge in the case of the HgTe NPLs. The full width at half maximum (FWHM) of the spectrum is also reported by fitting a gaussian shaped spectra to the excitonic resonance. The FWHM is connected to the coupling to phonons. We fit the FWHM using the expression $FWHM = \Gamma_0 + AT + Bn_{LO}(T)$ where Γ_0 is the zero temperature residual linewidth, A is the coupling to the acoustic phonon and $n_{LO}(T)$ is the Bose-Einstein distribution describing the thermal population of optical phonons.[13] Assuming a value of 123 cm-1 (15.3 meV) for the energy of the LO phonon in HgTe[14], we have determined $\Gamma_0 = 39.5$ meV, A=1.08 µeV.K^{-1}, and B = 15.8 meV.

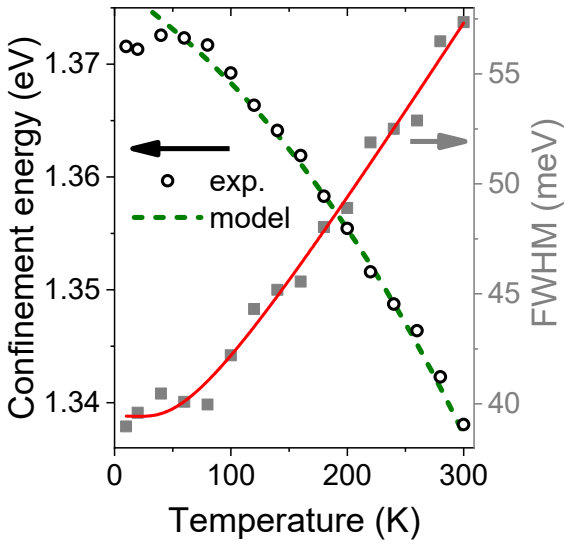

Figure S 12 Confinement energy and the full width at half maximum (FWHM) as a function of temperature for HgTe NPLs capped with Br-OLA. The green dashed curve is from the simple (3+1)-band model. The red curve is a fit of the experimental data using the expression $FWHM = \Gamma_0 + AT + Bn_{LO}(T)$.

The temperature dependence of the NPL confinement energy is simulated (dash green curve) accounting for the fitting only of $\frac{\partial E_{gC}}{\partial T} = -2.4$ meV.K^{-1}. This sets the temperature rate at which the second conduction band lowers its energy with increasing temperature. This thermal parameter is thus straightforwardly extracted from the temperature dependent spectroscopy and used as is in the rest of the simulations.

4.5 Detailed discussion on the effect of pressure, notably at low energies (≈ 0.5–0.7 eV)

The simple model assumes constant pressure potential $\frac{\partial E_g}{\partial P}$ and $\frac{\partial E_{gC}}{\partial P}$ for the band gaps in all the simulations. However, the confinement energy $E_G(P)$ exhibits the change in slopes depending on the energy of the HgTe nanoparticles, due to confinement. Whereas for HgTe NPLs, a slope of $\frac{dE_G}{dP} \simeq 100$ meV/GPa is predicted at high energy around 1.5 eV, for low energy nanocrystals around 0.5–0.7 eV, a reduced slope of $\frac{dE_G}{dP} \simeq 60$ meV/GPa is calculated, in good agreement with the measurements as depicted in Figure S 13a. The relative variation of E_G with pressure is however larger for larger nanoparticles, as reported in Figure S 13b. The latter figure also illustrates what the measurements did not show, i.e. the constant relative confinement energy variation with pressure at high energy around 1.1 eV – 1.5 eV, see the grouped lines in Figure S12b.

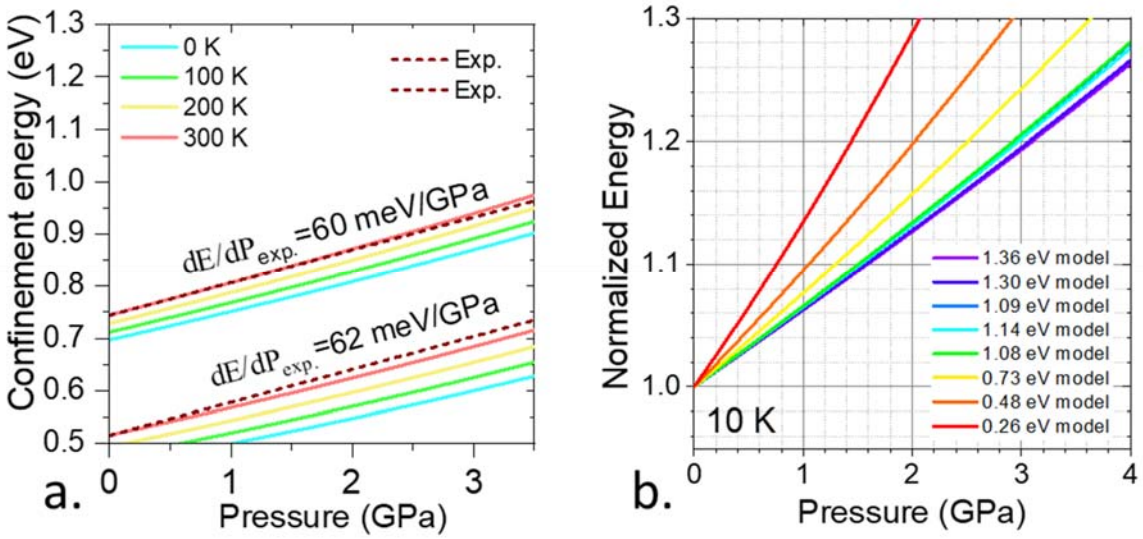

Figure S 13a. Simulated confinement energy $E_G(P)$ as a function of pressure P for various temperature T and for 2 confinement energies at 300 K of 0.515 eV and 0.744 eV. The dotted lines represent measured experimental slopes from Ref. [15] for NCs at the same 2 energies. b. Simulated confinement energies as a function of pressure for various NCs energies at 10 K. The energies are normalized to their value at zero pressure.

4.6 Realistic 14-band k.p model

Introduction. The spin-orbit interaction in HgTe around 0.775 eV is much larger than the band gap $E_G = 0.31\ eV$ (see Table 1 in the main text). A priori the spin-orbit interaction cannot be neglected. There is also a group of 6 bands higher in energy, referred to as the second conduction bands, close the first conduction band ≈3-4 eV above. The simple effective model has shown the importance of the second conduction bands. We check these interpretation and conclusion here with a more realistic and complete model.

14-band k.p matrix. The 14-band k.p model accounts for these features in details. The model is described in details in Ref. 16, in the case of O_h symmetric group. HgTe is a crystal of F $\bar{4}$3m symmetry without inversion center corresponding to T_d symmetry for the group representations of the zone center Bloch functions. In addition of E_p and $E_{pC} = E_{PX}$ interaction matrix elements, we therefore add the third interaction energy $E_{pV} = E'_p$ between the valence Γ_6 and Γ_8/Γ_7 Bloch functions of the second conduction band. A third spin-orbit coupling term Δ' between the valence and conduction Γ_8/Γ_7 Bloch functions is also added. Due to confinement, we restrict the matrix for wavevectors along the $\Gamma - X$ direction of the Brillouin zone: $\vec{k} = (0,0,k_z)$. We also set aside the perturbative interaction terms with bands outside the basis set, hence the matrix is said to be written at first order. Note that going to the second order in the 14-band k.p model, projecting the influence of remote bands outside of the state basis inside the 14x14 matrix, would not help because of the too high sensitivity of the dispersion at large k with temperature and pressure (not shown).

We write the matrix on a 14 basis states belonging to $\Gamma_6, \Gamma_8, \Gamma_7$ representations of T_d symmetry group. In this case the basis states and 14-band hamiltonian read:

	Γ_8			Γ_7		Γ_8				Γ_7		Γ_6	
	HH_C	LH_C		HH_C	SO_C		HH	LH		HH	SO		E_V	
	$\left\|\frac{3}{2},\frac{3}{2}\right\rangle_c$	$\left\|\frac{3}{2},\frac{1}{2}\right\rangle_c$	$\left\|\frac{3}{2},-\frac{1}{2}\right\rangle_c$	$\left\|\frac{3}{2},-\frac{3}{2}\right\rangle_c$	$\left\|\frac{1}{2},\frac{1}{2}\right\rangle_c$	$\left\|\frac{1}{2},-\frac{1}{2}\right\rangle_c$	$\left\|\frac{3}{2},\frac{3}{2}\right\rangle$	$\left\|\frac{3}{2},\frac{1}{2}\right\rangle$	$\left\|\frac{3}{2},-\frac{1}{2}\right\rangle$	$\left\|\frac{3}{2},-\frac{3}{2}\right\rangle$	$\left\|\frac{1}{2},\frac{1}{2}\right\rangle$	$\left\|\frac{1}{2},-\frac{1}{2}\right\rangle$	$\left\|\frac{1}{2}\right\rangle$	$\left\|-\frac{1}{2}\right\rangle$
HH_C	$\Delta_C + E_{gC}$	0	0	0	0	0	$\frac{\Delta'}{3}$	0	$\frac{P_C k_z}{\sqrt{3}}$	0	0	$\sqrt{\frac{2}{3}} P_C k_z$	0	0
LH_C	0	$\Delta_C + E_{gC}$	0	0	0	0	0	$\frac{\Delta'}{3}$	0	$\frac{P_C k_z}{\sqrt{3}}$	0	0	$\sqrt{\frac{2}{3}} k_z P_V$	0
	0	0	$\Delta_C + E_{gC}$	0	0	0	$-\frac{P_C k_z}{\sqrt{3}}$	0	$\frac{\Delta'}{3}$	0	0	0	0	$\sqrt{\frac{2}{3}} k_z P_V$
HH_C	0	0	0	$\Delta_C + E_{gC}$	0	0	0	$-\frac{P_C k_z}{\sqrt{3}}$	0	$\frac{\Delta'}{3}$	$\sqrt{\frac{2}{3}} P_C k_z$	0	0	0
SO_C	0	0	0	0	E_{gC}	0	0	0	0	$-\sqrt{\frac{2}{3}} P_C k_z$	$-\frac{2\Delta'}{3}$	0	$\frac{k_z P_V}{\sqrt{3}}$	0
	0	0	0	0	0	E_{gC}	$-\sqrt{\frac{2}{3}} P_C k_z$	0	0	0	0	$-\frac{2\Delta'}{3}$	0	$-\frac{k_z P_V}{\sqrt{3}}$
HH	$\frac{\Delta'}{3}$	0	$-\frac{P_C k_z}{\sqrt{3}}$	0	0	$-\sqrt{\frac{2}{3}} P_C k_z$	0	0	0	0	0	0	0	0
LH	0	$\frac{\Delta'}{3}$	0	$-\frac{P_C k_z}{\sqrt{3}}$	0	0	0	0	0	0	0	0	$\sqrt{\frac{2}{3}} P k_z$	0
	$\frac{P_C k_z}{\sqrt{3}}$	0	$\frac{\Delta'}{3}$	0	0	0	0	0	0	0	0	0	0	$\sqrt{\frac{2}{3}} P k_z$
HH	0	$\frac{P_C k_z}{\sqrt{3}}$	0	$\frac{\Delta'}{3}$	$-\sqrt{\frac{2}{3}} P_C k_z$	0	0	0	0	0	0	0	0	0
SO	0	0	0	$\sqrt{\frac{2}{3}} P_C k_z$	$-\frac{2\Delta'}{3}$	0	0	0	0	0	$-\Delta$	0	$\frac{P k_z}{\sqrt{3}}$	0
	0	0	0	0	0	$-\frac{2\Delta'}{3}$	0	0	0	0	0	$-\Delta$	0	$-\frac{P k_z}{\sqrt{3}}$
E_V	0	$\sqrt{\frac{2}{3}} k_z P_V$	0	0	$\frac{k_z P_V}{\sqrt{3}}$	0	0	$\sqrt{\frac{2}{3}} P k_z$	0	0	$\frac{P k_z}{\sqrt{3}}$	0	$-E_g$	0
	0	0	$\sqrt{\frac{2}{3}} k_z P_V$	0	0	$-\frac{k_z P_V}{\sqrt{3}}$	0	0	$\sqrt{\frac{2}{3}} P k_z$	0	0	$-\frac{P k_z}{\sqrt{3}}$	0	$-E_g$

(S7)

$$+\left(\frac{1}{6}\sqrt{4\left(\Delta'\right)^2+9\left(\Delta_C+\mathrm{E_{gC}}\right)^2}-\frac{1}{2}\left(\Delta_C+\mathrm{E_{gC}}\right)\right)\mathrm{Id}_{14} \quad \text{(S8)}$$

$$+\frac{\hbar^2k^2}{2m_0}\mathrm{Id}_{14} \quad \text{(S9)}$$

with E_g, E_{gC} 2 band gaps, $\Delta, \Delta_C, \Delta'$ 3 spin-orbit couplings, $P=\sqrt{\frac{E_p\hbar^2}{2m_0}}$, $P_C=\sqrt{\frac{E_{pC}\,\hbar^2}{2m_0}}$ and $P_V=\sqrt{\frac{E_{pV}\,\hbar^2}{2m_0}}$ 3 interaction matrix elements, Id_{14} the 14x14 identity matrix , $\hbar=\frac{h}{2\pi}$ the reduced Planck constant, m_0 the bare electron mass, Γ_i representation double group symmetry from Ref [17] notation, HH (heavy hole), LH (light hole), SO (spin-orbit), C index (conduction) notations in this SI. The constant term (S8) corresponds to the LH eigenenergy of (S7) at $\vec{k}=(0,0,0)$ setting the edge of LH and HH bands of the hamiltonian (S7)+(S8)+(S9) at 0 eV energy. Note that the state basis are strict eigenstates of the hamiltonian at $k=0$ only if the Δ' coupling is vanishing. If Δ' is non-zero, the input band gaps E_g, E_{gC} and spin-orbit terms Δ, Δ_C cannot be directly read in the dispersion at the zone center. The values are provided in Table 1 in the main text.

Energy dispersion. The eigen energies $E(k)$ of the hamiltonian are reported for each k along $\Gamma-X$ near the Γ Brillouin zone center in Figure S 14a. The dispersion of the LH conduction band exhibits an effective mass of $m^*_{LH}=0.013m_0$ upwards and the HH valence band $m^*_{HH}=0.69m_0$ downwards. The confinement energy is therefore mainly the result of confinement in the conduction band, with a small contribution from the valence band for not too large k. This justifies the static HH valence band considered in the simple model. The validity of the first order 14-band k.p model is limited to a small fraction of the Brillouin zone (k≈0.1-0.2 2π/a).

Three parameter values can be considered a priori surprising: smaller E_{gC} = 2.5 eV than ∼3–4 eV of LDA-QSGW calculations[7], E_{pV}=10 eV and $\Delta'=-1.5\ eV$ both vanishing in O_h crystal with inversion center and so expected to be small for T_d symmetry group without inversion center. These 3 values are debatable. Due to the non-diagonal hamiltonian at $k=0$, the band gap between LH and SO_C bands is actually 2.9 eV, close to the LDA 3 eV value. $E_{pV}=E'_p$ is well known to vary between 0.065 and 11 eV in GaAs, though the 0.065 eV appears to be a more realistic and satisfying value.[18] Note that depending on the zinc-blende III-V semiconductor, E_{pV} is found between 0.0095 eV (AlP) and 0.47 eV (GaSb).[19] In the same Ref. [19], $\Delta'=\Delta^-$ is either positive or negative with values between -0.41 eV and 0.11 eV so a value of -1.5 eV remains roughly of the same order of magnitude. Adding more bands to the model may give a better insight on the origin and validity of these parameters.

In Figure S 15b the dispersion relation $E_G(k)$ for the confinement energy is clearly parabolic at very small k corresponding to less than 1% 2π/a away from the Brillouin zone center, and clearly linear for larger k. The linearity is the signature of strong contribution of remote bands to the dispersion relation.

Effect of temperature. Figure S 14b-c mimic the Figures 1, Figure 5a and Figure 6a in the main text for the simplified model and result from the variation of the 2 band gaps E_g and E_{gC} with temperature and pressure. The crossing of the LH conduction band dispersion with temperature is transferred to the E_G confinement energy, as shown in Figure S14b.

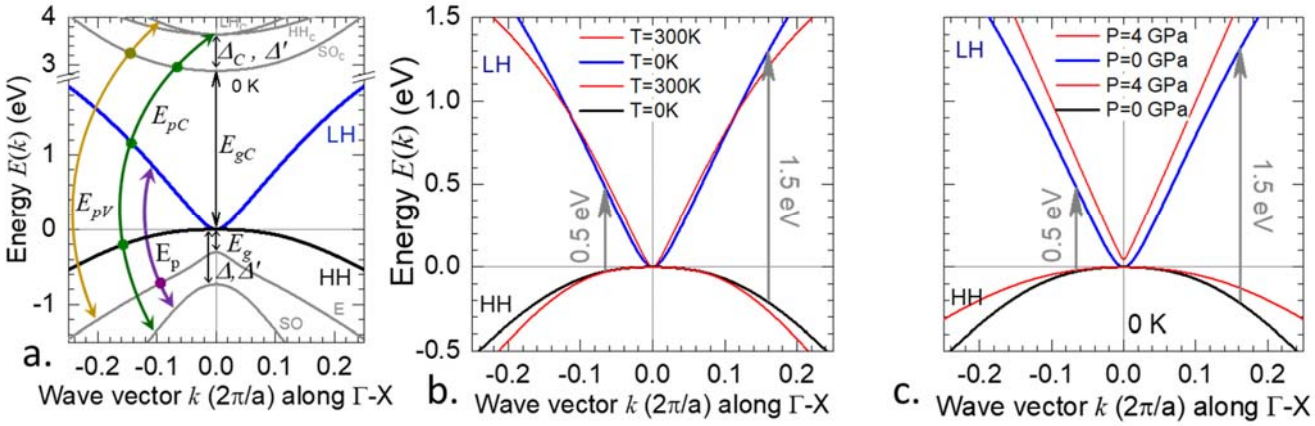

Figure S 14a. Simulated dispersion $E_i(k)$ for the 14 bands of the k.p model. All the bands are spin degenerated twice due to spin. The 3 band gaps E_g, E_{gC} and E_{gV} and the 3 spin-orbit interactions $\Delta, \Delta_C, \Delta'$ and the 3 interaction elements E_p, E_{pC} and E_{pV} between the groups of bands are indicated. The confinement energy is the energy difference between the light hole like (LH) and heavy hole like (HH) bands. b. Effect of temperature simulated on the electronic structure. c. Effect of pressure on the electronic structure at 0 K.

To analyze in more details the difference between the simple model and the 14-band model, we recalculated Figure S11, Figure S10d, Figure 5c, Figure 3d, of the simple model, in Figure S 15a, b, c and d respectively with the 14-band model. The overall agreement with experimental data is essentially due to the chosen value for the three surprising parameters E_{gC}, $E_{pV} = E_p{}'$, Δ'. However, some discrepancies remain. The main difference comes at high energy, as shown in Figure S 15a where the effect of temperature on the energy shows significant evolution with increasing temperature. This is attributed to the limited validity of the 14-band model at large $k \approx 15\%\ 2\pi/a$ corresponding to these relatively high energies ≈1.5 eV.

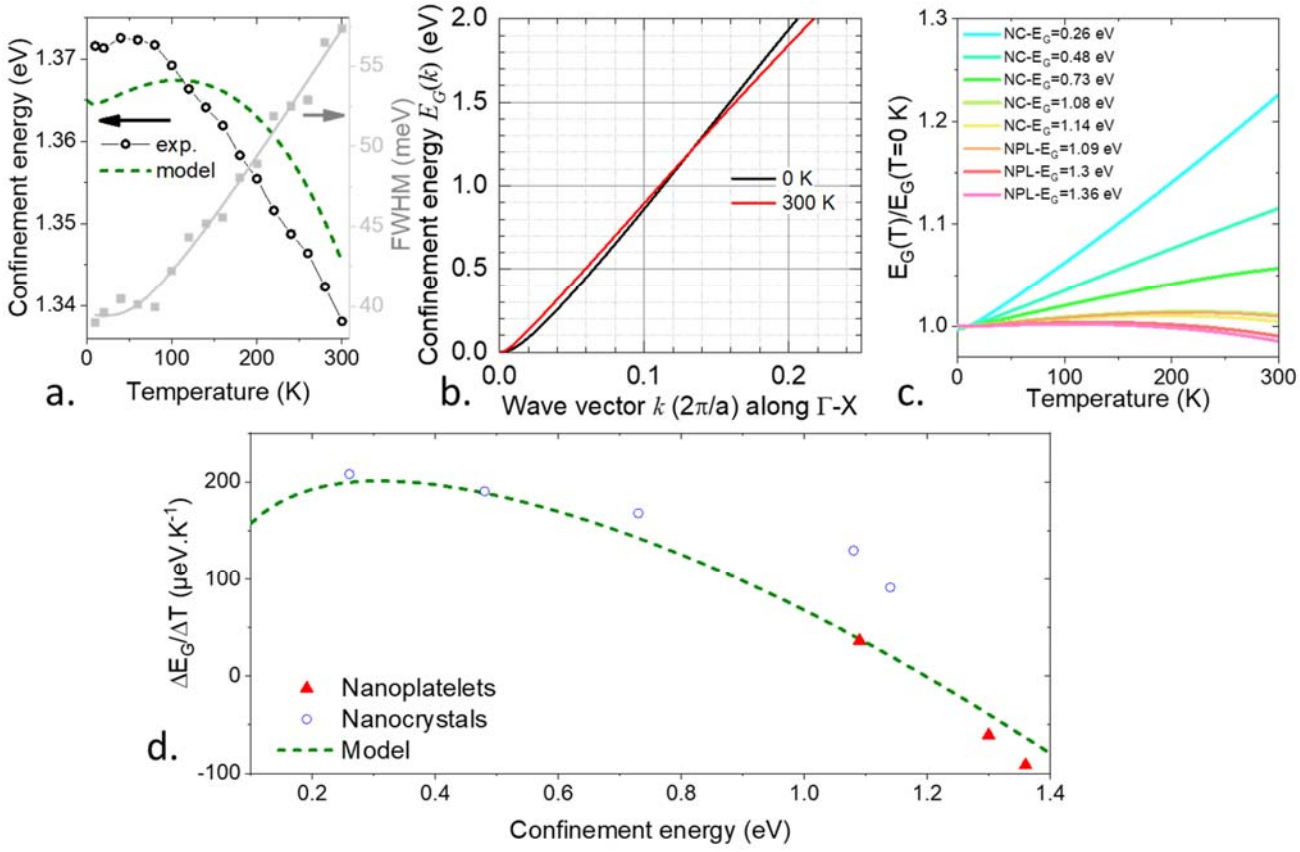

Figure S 15a. The green dashed line represents the simulated confinement energy $E_G(T)$ as a function of temperature. It is compared to the experimental data reported in the main text in Fig. 4a. b. Simulated dispersion relation $E_G(k)$ for the confinement energy for 2 temperatures of 0 K and 300 K. c. Simulated confinement energy as a function of temperature normalized to their value at 0 K and reported for various energy in HgTe nanocrystals and nanoplatelets. It is to be compared to Figure 3c in the main text. d. The green line is the simulated confinement energy variation (slope) between 0 K and 300 K. It is compared to the experimental measurements. All 3 Figures a, c, and d are in correspondence to Fig. 3 a, c, and d in the main text and can be superimposed with exact scale match.

Effect of pressure. In Figure S 16a, when pressure increases, HgTe E_g band gap shrinks and even becomes negative, indicating that the true band gap opens in the HgTe relation dispersion $E(k = 0)$ at 3.5 GPa. The relative variation of the confinement energy is similar in the 14-band model reported in Figure S 16b and in the simple model Figure S 13b. The same analysis applies. However quantitatively at high energy (> 1 eV), strong differences in slopes are simulated between the two models.

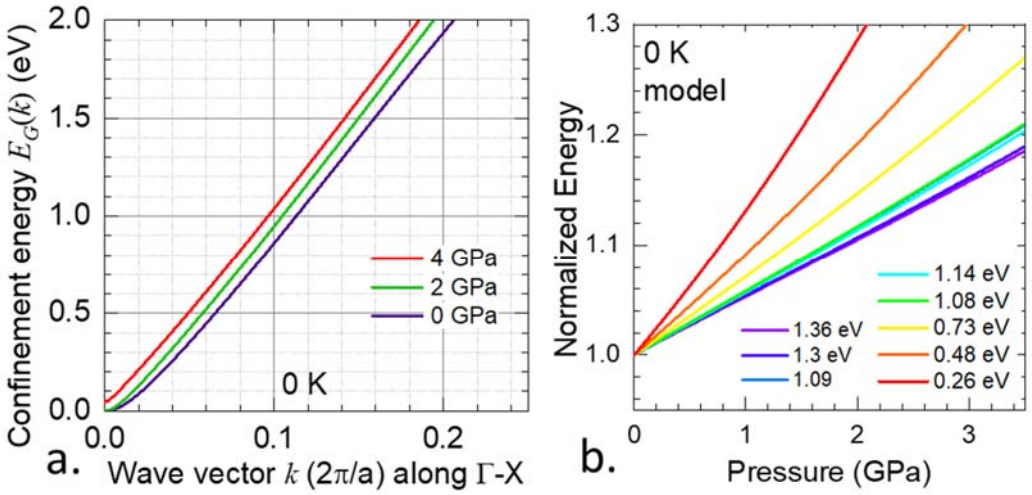

Figure S 16a. Simulated dispersion relation of the confinement energy $E_G(k)$ or various hydrostatic pressure P. b. Simulated confinement energy as a function of pressure normalized to their value at 0 K and 0 GPa and reported for various energy in HgTe nanocrystals and nanoplatelets.

To better analyze this pressure difference between the two models, Figure S 17a shows that the simulation for HgTe nanoplatelets at high pressure and high energy simulated confinement is qualitatively corrected but quantitatively incorrect. This is due to the large value of the discretized k wave vector. Around $16\% \text{ x } 2\pi/a$ away from the Brillouin zone center along $\Gamma - X$, the 14-band k.p model is no longer valid quantitatively. However, at low energy, agreement with experiment is still satisfying, for the opposite reason at $k \approx 6\% \text{ x } 2\pi/a$ of Γ as seen in Figure S 17b. Overall one exhibits the transition between validity and non-validity in Figure S 17c where 3 symbols corresponding to measurements are reported for comparison.

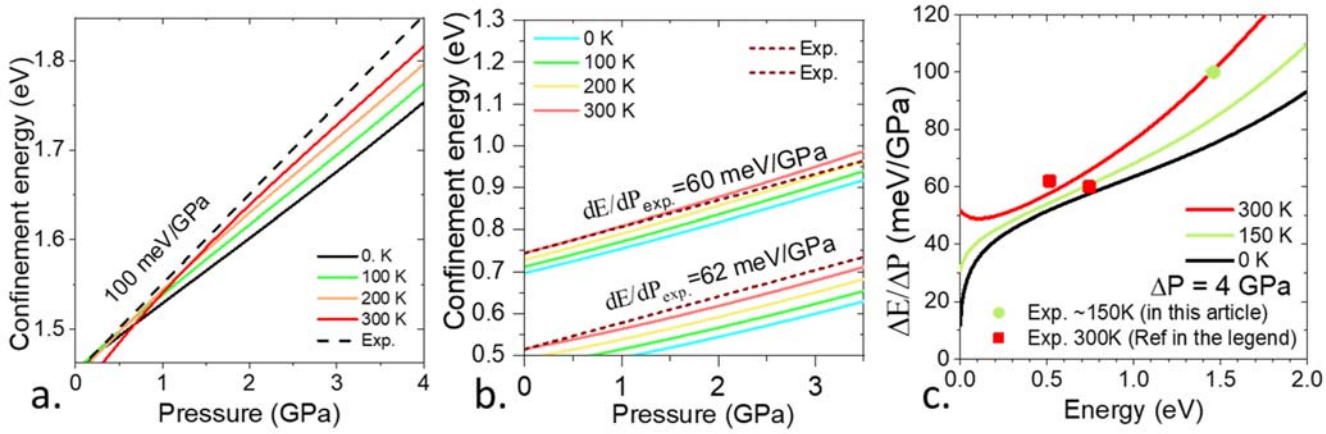

Figure S 17 a. Simulated confinement energy $E_G(P)$ as a function of the hydrostatic pressure P for various temperature T for HgTe nanoplatelets of energy of 1.51 eV at 0 K and 0 GPa. b. Idem a. but for HgTe nanocrystals energy of 0.515 eV and 0.744 eV at 0 K and 0 GPa. c. Simulated confinement energy variation (slope) between 0 GPa and 4 GPa as a function of the nanoparticle energy. The symbols are the experimental measurements of that slope reported in the main text (light green disk) at high energy and in Ref. [15] (red square) at low energy.

Conclusion on the 14-band k.p model. The 14-band model is a realistic model to predict the dispersion relation $E(k)$ near the zone center. Providing some debatable fitting of input energies and interaction matrix elements with values expected or reported elsewhere, either experimental or theoretical in the literature, reasonable agreement is obtained with the experimental data. However, there are still some discrepancies at high energy. The 14-band k.p model still remains limited to around $10\% - 15\%$ of the Brillouin zone. The inclusion of more bands will certainly extend the validity at high energy and possibly accounts better for the simultaneous energy, temperature and pressure dependences.

4.7 Conclusion

By comparing high energy NPLs with lower absorption energy NCs, we were able to probe experimentally a large range of energies over nearly a decade, from 0.26 eV up to 1.8 eV. We have also probed the confinement energy through absorption resonance systematically as a function of temperature and pressure, both for NPLs and NCs in the zinc-blende phase. We present that temperature and stress HgTe potentials can be extracted from the tuning of the models to the experimental spectroscopies.

The confrontation with the modeling suggests that the energy variations are the results of the electronic structure specific dispersion relation of bulk HgTe. The observed energy variations are related to the strong non-parabolic character of $E_G(k)$. The data imply that modellings including at least the second band are necessary to describe the nanoparticle electronic states, especially for strongly confining NPLs. The second conduction bands play a key role at high energy. A 2-band approach, or even an 8-band model, traditional and usually useful in k.p modeling of nanostructures, appears as not sufficient in this case. The inclusion of more bands, even more than 14 bands, would help to improve the description of temperature and pressure dependence of high energy dispersion and states.

5. REFERENCES

(1) Izquierdo, E.; Robin, A.; Keuleyan, S.; Lequeux, N.; Lhuillier, E.; Ithurria, S. Strongly Confined HgTe 2D Nanoplatelets as Narrow Near-Infrared Emitters. *J. Am. Chem. Soc.* **2016**, *138*, 10496–10501.

(2) Geiregat, P.; Houtepen, A. J.; Sagar, L. K.; Infante, I.; Zapata, F.; Grigel, V.; Allan, G.; Delerue, C.; Van Thourhout, D.; Hens, Z. Continuous-Wave Infrared Optical Gain and Amplified Spontaneous Emission at Ultralow Threshold by Colloidal HgTe Quantum Dots. *Nat. Mater.* **2018**, *17*, 35–42.

(3) Keuleyan, S.; Lhuillier, E.; Guyot-Sionnest, P. Synthesis of Colloidal HgTe Quantum Dots for Narrow Mid-IR Emission and Detection. *J. Am. Chem. Soc.* **2011**, *133*, 16422–16424.

(4) Śniadower, L.; Psoda, M.; Gałązka, R. R. X-Ray Measurements of Lattice Dilatation in HgTe. *Phys. Status Solidi B* **1968**, *28*, K121–K123.

(5) Dufour, M.; Qu, J.; Greboval, C.; Méthivier, C.; Lhuillier, E.; Ithurria, S. Halide Ligands To Release Strain in Cadmium Chalcogenide Nanoplatelets and Achieve High Brightness. *ACS Nano* **2019**, *13*, 5326–5334.

(6) Düz, I.; Erdem, I.; Ozdemir Kart, S.; Kuzucu, V. First Principles Investigations of HgX (X=S, Se and Te). *Arch Mater Sci Eng* **2016**, *79*, 5–11.

(7) Svane, A.; Christensen, N. E.; Cardona, M.; Chantis, A. N.; van Schilfgaarde, M.; Kotani, T. Quasiparticle Band Structures of β-HgS, HgSe, and HgTe. *Phys. Rev. B* **2011**, *84*, 205205.

(8) Luttinger, J. M.; Kohn, W. Motion of Electrons and Holes in Perturbed Periodic Fields. *Phys. Rev.* **1955**, *97*, 869–883.

(9) Laurenti, J. P.; Camassel, J.; Bouhemadou, A.; Toulouse, B.; Legros, R.; Lusson, A. Temperature Dependence of the Fundamental Absorption Edge of Mercury Cadmium Telluride. *J. Appl. Phys.* **1990**, *67*, 6454–6460.

(10) Chen, M.; Guyot-Sionnest, P. Reversible Electrochemistry of Mercury Chalcogenide Colloidal Quantum Dot Films. *ACS Nano* **2017**, *11*, 4165–4173.

(11) Allan, G.; Delerue, C. Tight-Binding Calculations of the Optical Properties of HgTe Nanocrystals. *Phys. Rev. B* **2012**, *86*, 165437.

(12) Bir, G. L.; Pikus, G. E. *Symmetry and Strain- Induced Effects in Semiconductors*, Wiley.; Wiley: New York, 1974.

(13) Itoh, T.; Furumiya, M. Size-Dependent Homogeneous Broadening of Confined Excitons in CuCl Microcrystals. *J. Lumin.* **1991**, *48–49*, 704–708.

(14) Goubet, N.; Jagtap, A.; Livache, C.; Martinez, B.; Portalès, H.; Xu, X. Z.; Lobo, R. P. S. M.; Dubertret, B.; Lhuillier, E. Terahertz HgTe Nanocrystals: Beyond Confinement. *J. Am. Chem. Soc.* **2018**, *140*, 5033–5036.

(15) Livache, C.; Goubet, N.; Gréboval, C.; Martinez, B.; Ramade, J.; Qu, J.; Triboulin, A.; Cruguel, H.; Baptiste, B.; Klotz, S. *et al* Effect of Pressure on Interband and Intraband Transition of Mercury Chalcogenide Quantum Dots. *J. Phys. Chem. C* **2019**, *123*, 13122–13130.

(16) El kurdi, M.; Fishman, G.; Sauvage, S.; Boucaud, P. Comparison between 6-Band and 14-Band k·p Formalisms in SiGe/Si Heterostructures. *Phys. Rev. B* **2003**, *68*, 165333.

(17) Koster, G. F.; Dimmock, J. O.; Wheeler, G.; Statz, R. G. Properties of the Thirty-Two Point Groups. M.I.T.Press, Cambridge, Massachusetts, U.S.A; 1963.

(18) Richard, S.; Aniel, F.; Fishman, G. Energy-Band Structure of Ge, Si, and GaAs: A Thirty-Band k.p Method. *Phys. Rev. B* **2004**, *70*, 235204.

(19) Jancu, J.-M.; Scholz, R.; de Andrada e Silva, E. A.; La Rocca, G. C. Atomistic Spin-Orbit Coupling and k·p Parameters in III-V Semiconductors. *Phys. Rev. B* **2005**, *72*, 193201.